Ultralong Phosphorescence of Water-Soluble Organic Nanoparticles for In Vivo Afterglow Imaging

Zhen, Xu; Tao, Ye; An, Zhongfu; Chen, Peng; Xu, Chenjie; Chen, Runfeng; Huang, Wei; Pu, Kanyi

2017

Zhen, X., Tao, Y., An, Z., Chen, P., Xu, C., Chen, R., et al. (2017). Ultralong Phosphorescence of Water-Soluble Organic Nanoparticles for In Vivo Afterglow Imaging. Advanced Materials, 29(33), 1606665-.

https://hdl.handle.net/10356/83793

https://doi.org/10.1002/adma.201606665

Submitted to ADVANCED MATERIALS

DOI: 10.1002/adma.((please add manuscript number))
Article type: Communication

Ultralong Phosphorescence of Water-soluble Organic Nanoparticles for *In Vivo* Afterglow Imaging

By *Xu Zhen*,[1] *Ye Tao*,[2] *Zhongfu An*,[3] *Peng Chen*,[1] *Chenjie Xu*,[1] *Runfeng Chen*,[2,*] *Wei Huang*,[3,*] and *Kanyi Pu*[1,*]

[1] Dr. X. Zhen, Prof. P. Chen, Prof. C. Xu, Prof. K. Pu
School of Chemical and Biomedical Engineering, Nanyang Technological University
Singapore 637457
Email: kypu@ntu.edu.sg

[2] Y. Tao, Prof. R. Chen
Key Laboratory for Organic Electronics and Information Displays (KLOEI) & Institute of Advanced Materials (IAM), Synergistic Innovation Center for Organic Electronic and Information Displays (SICOEID), Nanjing University of Posts and Telecommunications
Nanjing, 210023, China
Email: iamrfchen@njupt.edu.cn

[3] Dr. Z. An, Prof. W. Huang
Key Laboratory of Flexible Electronics (KLOFE) &Institute of Advanced Materials (IAM), Jiangsu National Synergistic Innovation Center for Advanced Materials (SICAM), Nanjing Tech University
Nanjing 211816, China
Email: wei-huang@njtech.edu.cn

Keywords: afterglow, phosphorescence, molecular imaging, organic semiconducting nanoparticles, lymph node imaging

Optical imaging plays an indispensable role in biology and medicine,[1] and has been used in clinics for imaging-guided surgery.[2] Many optical agents such as organic dyes,[3] semiconductor quantum dots,[4] up-conversion nanoparticles,[5] carbon nanodots[6] and semiconducting polymer nanoparticles[7] have been applied to *in vivo* optical imaging. However, the requirement of external light excitation during imaging process can induce strong tissue autofluorescence,[8] consequently compromising imaging sensitivity and specificity in living subjects. Although bioluminescence[9] and Cerenkov probes[10] eliminate the need of light excitation and thus circumvent the issue of autofluorescence, they usually require specific enzymes and substrates or radioactive isotopes to produce light emission, which partially complicate their imaging applications.

Afterglow or persistent luminescence has been attracting attention for molecular imaging, because it can last for a certain amount of time after removal of illumination source, permitting *in vivo* imaging without real-time external excitation.[11] However, only several persistent luminescent nanoparticles have been reported for *in vivo* optical imaging,[11] all of which use rare-earth metals or heavy metals such as europium, dysprosium and chromium to create the energy traps to store and slowly release the excitation energy for long-lived luminescence. Although these doping content of rare-earth metals or heavy metals is low in persistent luminescent nanoparticles,[11] the ions of those metal are known to be toxic,[12] biocompatibility of current inorganic persistent luminescent nanoparticles should be concerned in the long term. To fully explore the applications of persistent luminescence in life science, development of persistent luminescence nanoparticles based on benign organic ingredients becomes essential, which remains to be revealed.

The key challenge in the design of organic nanoparticles for afterglow imaging lies in the creation of energy traps to prolong the luminescence time, as organic dyes generally have the characteristic of ultrafast deactivation due to the highly active excited states.[13] Although either inorganic metals (such as Ir^{3+} and Pt^{2+}) or special organic moieties (such as aromatic aldehyde,

heavy halogen and deuterated) can be integrated into organic molecules to enhance the transition of singlet-to-triplet states,[13] the resulted compounds can only show prolonged luminescence lifetimes under specific conditions such as inert atmospheres, solid crystal state and ultralow temperatures. In addition to those critical conditions that are less possible to be obeyed in biological systems, the non-water-soluble nature of these organic molecules further makes them incompetent for molecular imaging.

We herein report a top-down approach to synthesis water-soluble organic semiconducting nanoparticles (OSNs) with ultralong phosphorescence for *in vivo* afterglow imaging. The approach takes advantage of strong molecular packing of organic phosphorescent semiconducting dyes to generate aggregates within nanoparticles. Our previous report has revealed that H-aggregates can effectively stabilize the triplet excited states and lead to the formation of ultralong lived excitons for phosphorescence at room temperature (**Figure 1**).[14] Maximizing the formation of H-aggregates within nanoparticles is thus the key factor to generate prolonged phosphorescence. A top-down approach is used to synthesize the nanoparticles (OSNs-T) directly from the solid crystals of the organic phosphorescent semiconducting dyes, while a bottom-up approach (nanoprecipitation) is used to synthesize the nanoparticle with less aggregation (OSNs-B) from the homogeneously dissolved tetrahydrofuran (THF) solution of those dyes (**Figure 1**). To demonstrate the universal applicability of the proposed top-down approach in prolonging the lifetime of phosphorescence, a series of phosphorescent dyes including DPhCzT (OS1), CzPhF (OS2) and DClCzT (OS3) were synthesized (**Figures S1&S2**, Supporting Information) and transformed to water-soluble nanoparticles and tested for afterglow optical properties.

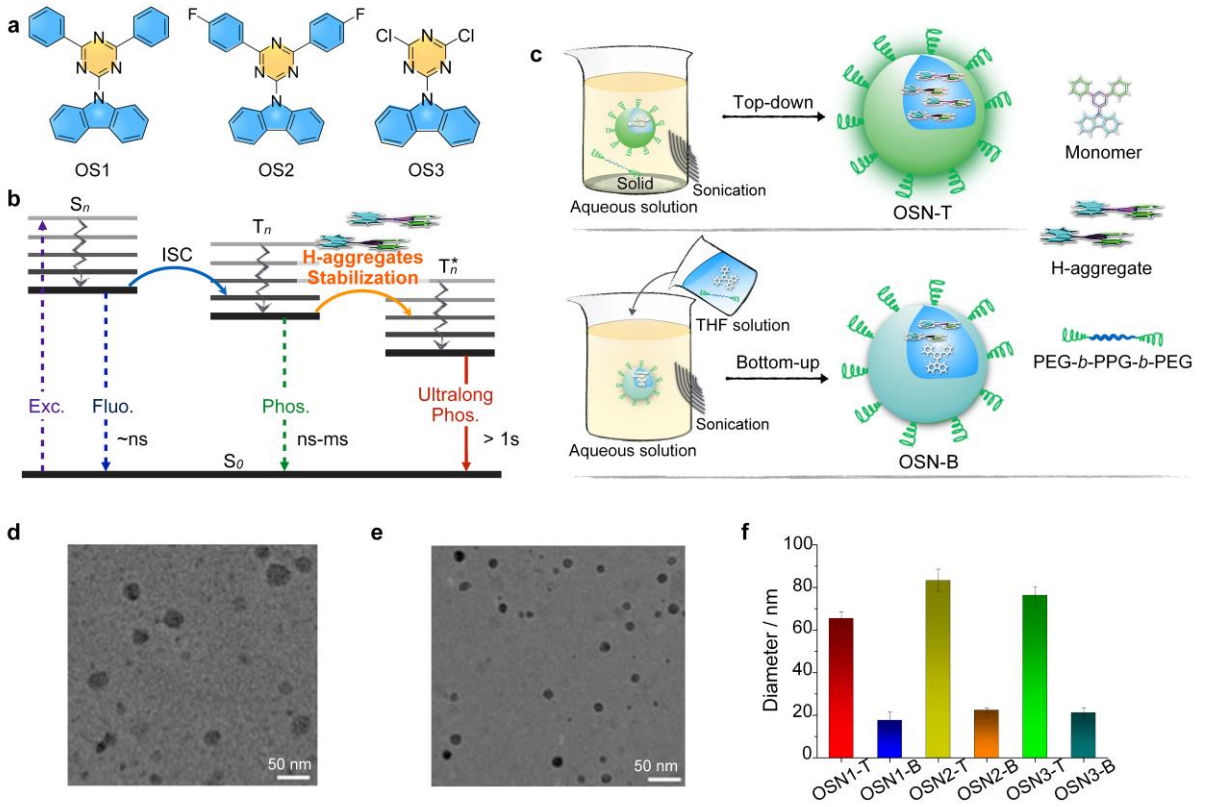

Figure 1. Design and characterization of OSNs for afterglow imaging. (**a**) Chemical structures of OS1, OS2 and OS3, respectively. (**b**) Proposed mechanism for the ultralong phosphorescence of OSNs based on formation of H-aggregates. (**c**) Top-down and Bottom-up routes to synthesize OSNs-T and OSNs-B, respectively. Representative TEM images of OSN1-T (**d**) and OSN1-B (**e**), respectively. (**f**) DLS of OSNs in 1×PBS (pH = 7.4).

To endow the OSNs with good aqueous solubility, an amphiphilic triblock copolymer, PEG-*b*-PPG-*b*-PEG, was used to stabilize nanoparticles in water during the sonication for both bottom-up and top-down approaches. Each pair of OSNs-T and OSNs-B are thus composed of the same phosphorescence dye. Despite having the same spherical morphology (**Figures 1d&1e**), OSNs-T have a larger hydrodynamic diameter of ~70-80 nm as compared to that of OSNs-B (~20 nm) (**Figure 1f**) due to the difference in synthetic approach. However, as a result of the same PEG coating, the zeta potentials of OSNs-T and OSNs-B are quite similar, which are -7.36±1.06 (OSN1-T), -8.24±0.45 (OSN2-T), -7.56±1.24 (OSN3-T), -4.84±0.49 (OSN1-B), -4.65±0.87 (OSN2-B) and -5.23±0.55 (OSN3-B) mV. No precipitation was observed for both OSNs after storage at 4 °C for weeks and their sizes remained nearly the same (**Figure S3**,

Supporting Information). Besides, no obvious cytotoxicity was detected for both nanoparticles (**Figure S4**, Supporting Information). The good aqueous stability and cytocompatibility of OSNs indicate their potential for biological applications.

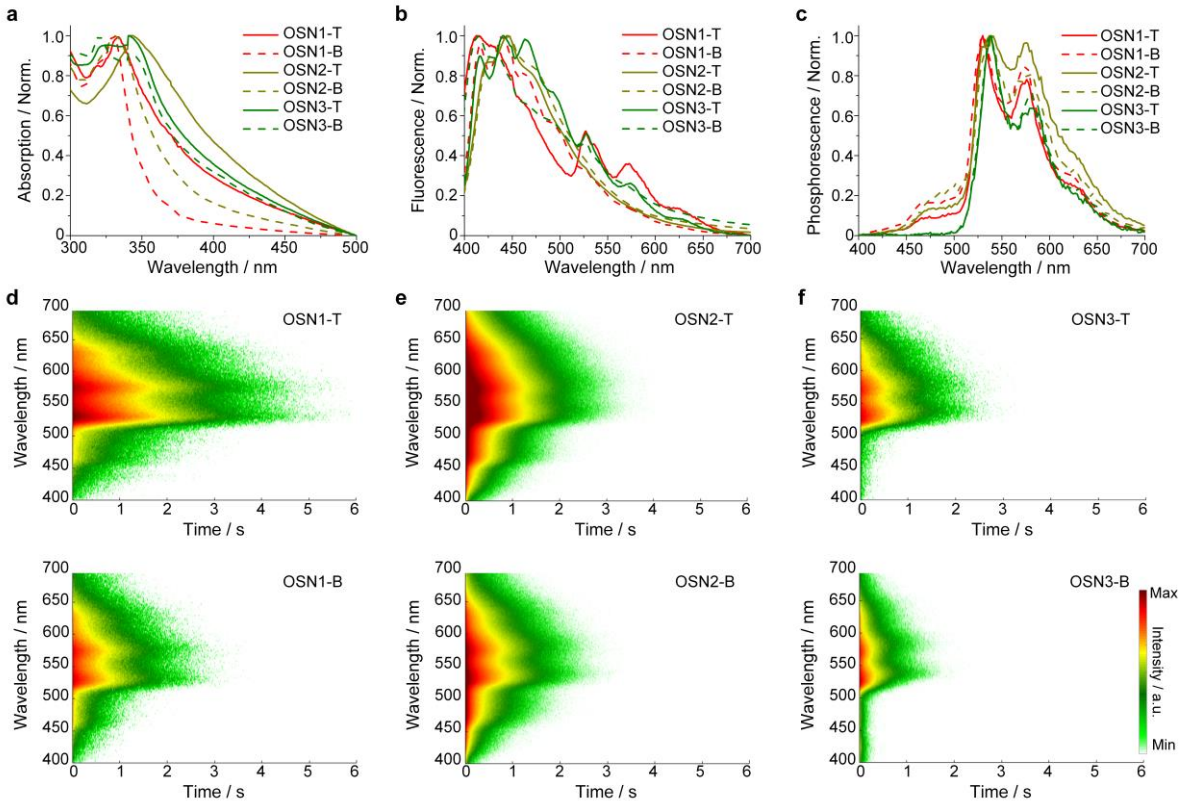

Figure 2. Optical characterization of OSNs. Normalized absorption (**a**), fluorescence (**b**), and phosphorescence (**c**) spectra of OSNs-T and OSNs-B in PBS. (**d, e, f**) Transient luminescence decay images of OSNs-T (top) and OSNs-B (down).

The optical properties of OSNs were studied and compared at pH = 7.4 in 1× phosphate buffered saline (PBS). For each pair of OSNs, the absorption spectrum of OSN-T is broader than that of OSN-B (**Figure 2a**), showing a strong tail extending to long-wavelength range. Besides, the absorption maxima are different from those in organic solvent (Figure S5, Supporting Information). For instance, both OSN1s have the dual absorption peaks at 320 and 330 nm (**Figure 2a**), which is different from the single absorption peak of OS1 at 325 nm in organic solvent. According to our previous experimental and theoretical studies, the blue-shifted absorption peak at 320 nm is assigned to the H-aggregation of OS1,[14] which can

prolong the luminesce lifetime of OS1 in solid state. The formation of H-aggregates during the aggregation of OS1 can be verified by the newly emerged and gradually enhanced absorption peak at 320 nm upon addition of the poor solvent (water) into the methanol solution of OS1 (**Figure S6**, Supporting Information). Furthermore, single crystal structure analysis (**Figure S7**, Supporting Information) reveals a large angle (θ) of 80.9º between the transition dipoles and interconnected axis; according to the exciton model reported previously,[15] this indicates the formation of H-aggregates as θ is larger than 54.7 º, which is a critical degree in determining H- or J-aggregation (Figure S7c). The broader absorption peak of OSN-T relative to that of OSN-B implies that the extent of molecular packing in OSN-T is stronger than that in OSN-B. This is consistent with the larger size of OSN-T, and can be rationalized by the fact that OSN-T is made directly from the solid crystals of the dyes, which better resembles the molecular packing of the dyes in solid states.

The steady-state photoluminescence spectra in **Figure 2b** show that the major fluorescence peaks of each pair of OSN-T and OSN-B are also nearly the same. However, as compared to OSNs-B, the fluorescence spectra of OSNs-T are more vibronic and broader, and their fluorescence quantum yields are lower (4.88% *vs* 9.84% for OSN1, 4.18% *vs* 4.35% for OSN2 and 8.7% *vs* 9.7% for OSN3). The fluorescence spectral profiles of OSNs-T are very similar to those of the thin films and crystals of the dyes (**Figures S8** and **S9**, Supporting Information), which again proves the stronger extent of molecular aggregation in OSNs-T relative to OSNs-B. Unlike fluorescence, the phosphorescence spectral profiles are quite similar for each pair of OSNs, featuring the major emission peak at ~530 nm with a tail extending to the near-infrared region (**Figure 2c**). In addition, the spectral profiles of OSN1 are identical to that of OS1 crystals (**Figure S9**, Supporting Information), suggesting that they are intrinsically originated from the same excited states. However, the phosphorescence quantum yields of OSNs-T (1.59% for OSN1-T, 1.70% for OSN2-T, and 1.90% for OSN3-T) are slightly lower than that of OSNs-

B (1.77% for OSN1-B, 1.86% for OSN2-B, and 3.50% for OSN3-B). The transient photoluminescence decay images also reveal that OSN-T decays much slower than the corresponding OSN-B does (**Figure 2d**). In fact, the life-time of phosphorescence for OSN1-T (861 ms), OSN2-T (354 ms) and OSN3-T (440 ms) is 1.75-, 1.29- and 1.77-times respectively longer than those for OSN1-B (492 ms), OSN2-B (275 ms) and OSN3-B (249 ms) (**Figure S10**, Supporting Information). The different phosphorescent behaviors of OSNs are attributed to the stronger molecular packing of OSNs-T that facilitates the formation of H-aggregates more than that of OSNs-B do. As confirmed in our previous study, H-aggregate has a lower energy level and can serve as the energy trap to stabilize the triplet excitons.[14] Additionally, the low-lying energy level of H-aggregate is disfavored for the radiative decay of the excitons, which further delays the phosphorescence. As a result of the stronger molecular packing of OSNs-T, the triple excitons are more stabilized for OSNs-T as compared with that for OSNs-B, leading to the longer life-time of the phosphorescence of OSNs-T. Thus, these results imply that although molecular packing decreases the luminescence quantum yields of OSNs for both fluorescence and phosphorescence, it helps prolong the life-time of phosphorescence to the time scale that is close to second, leading to the increased absolute luminescence brightness after removal of external light source. To the best of our knowledge, this has not been achieved before in aqueous solution from phosphorescence dyes.[11,13,14]

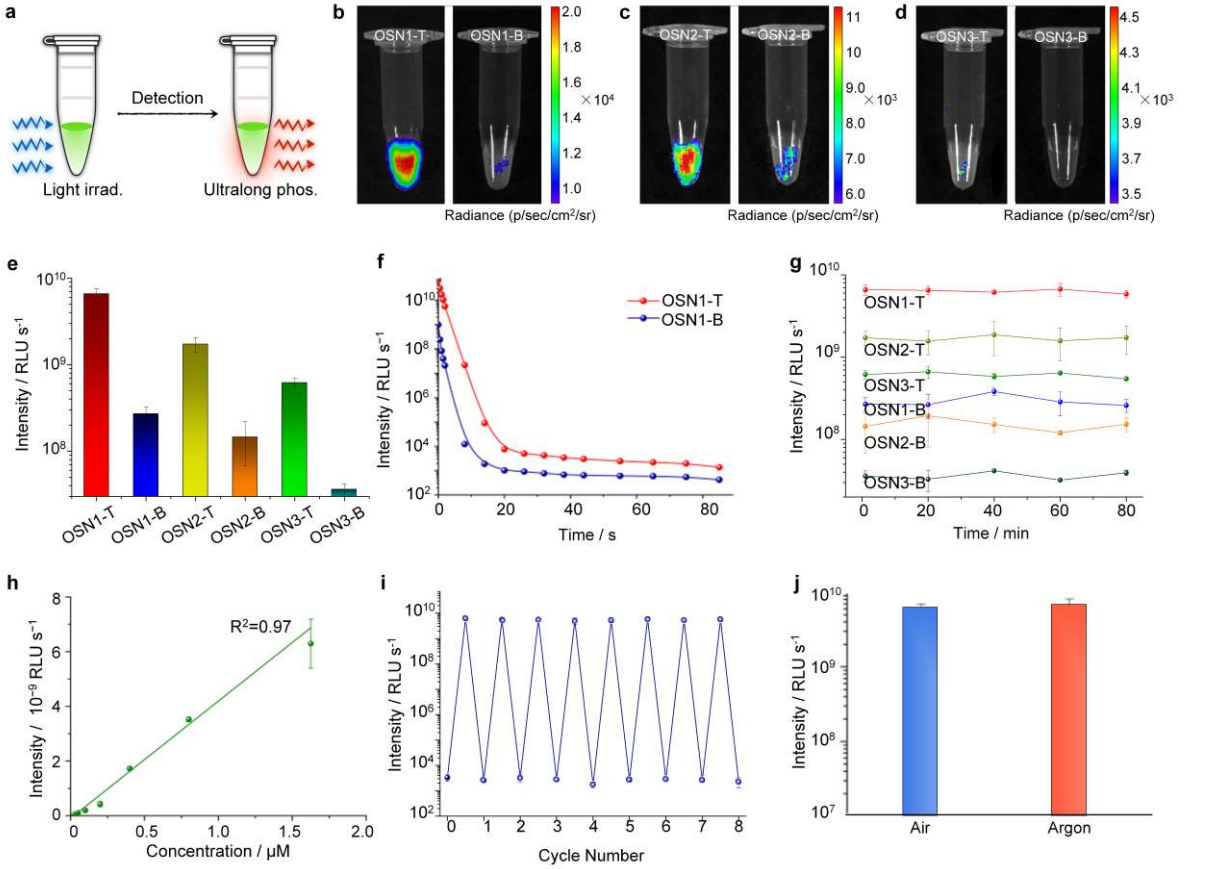

Figure 3. In vitro characterization of ultralong **phosphorescence of OSNs**. (**a**) Schematic illustration of activation and detection of ultralong phosphorescence in solution. (**b,c,d**) Ultralong phosphorescence images of OSNs solutions. The images were taken at t=10 s after removal of light illumination source. [OSN] = 1.6 μM in 1× PBS (pH = 7.4) (**e**) The ultralong phosphorescence intensities of OSNs. [OSN] = 1.6 μM in 1× PBS (pH = 7.4). (**f**) Time-dependent luminescence decay of ultralong phosphorescence of OSNs recorded after light irradiation for 1 min. The power density is 10 mW/cm^2. (**g**) The ultralong phosphorescence intensities of OSNs under continuous light irradiation for 80 min (the power density: 10 mW/cm^2). (**h**) The ultralong phosphorescence intensities as a function of the concentration of OSN1-T. (**i**) The ultralong phosphorescence intensities of OSN1-T solution as a function of the cycle number of light activation. (**j**) The ultralong phosphorescence intensities of OSN1-T solution purged with air or argon. Error bars were based on standard deviation (n=3).

To find out if the ultralong phosphorescence of OSNs after removal of external light source is qualified as ultralong phosphorescence for *in vivo* imaging, IVIS living imaging system was used to collect the photons and record the images under the bioluminescence mode where the light excitation is off during imaging process. The solutions of OSNs were first irradiated with

UV light for 1 min to activate nanoparticles, allowing the photon energy to be stored (**Figure 3a**). Then, releasing of the stored photon energy was detected and image acquisition was carried out after removal of light source (**Figure 3a**). As shown in **Figures 3b, 3c&3d**, the ultralong phosphorescence of OSNs-T can be easily detected even at t = 10 s after removal of light source; in contrast, the luminescence intensities of OSNs-B are very low under the same intensity scale. Among these OSNs-T, OSN1-T shows the strongest ultralong phosphorescence intensity (**Figure 3e**). The long-time luminesce decay curves further reveal that the ultralong phosphorescence of OSN1-T decays much slower than OSN1-B does (**Figure 3f**). In addition, the ultralong phosphorescence of OSNs remains nearly the same after continuous light irradiation for 80 min (**Figure 3g**), demonstrating their excellent photostability.

As OSN1-T has the highest ultralong phosphorescence among these OSNs, it is applied for the following *in vitro* and *in vivo* experiments. The ultralong phosphorescence of OSN1-T detected at t = 10 s post-excitation is in a good linear relationship with the nanoparticle concentration (**Figure 3h**), suggesting the probability for the quantitative conversion of luminescence signal into particle concentration. It can be repeatedly activated with no obvious loss of intensity (**Figure 3i**), showing the good optical stability and signal consistency of OSN1-T. This re-activatable luminescence should be useful for longitudinal detection and imaging. Additionally, the ultralong phosphorescence for the OSN1-T solution purged with argon shows no difference from the solution purged with air (**Figure 3j**), which indicates its inertness towards oxygen. Such an oxygen-inert luminescence characteristic is distinct from the conventional phosphorescence that can be quenched by oxygen, and could be attributed to the strong molecular packing within the nanoparticles that substantially minimizes the contact between the dye molecule and oxygen. Moreover, this optical feature should be beneficial to imaging in living organisms where oxygen is abundant.

The ability of OSNs for *in vivo* imaging was validated in living mice. After subcutaneous injection of nanoparticles into the dorsal area of mice, in-situ activation of ultralong

phosphorescence was conducted by irradiation with UV light for 1 min (**Figure 4a**). Note that the power density (10 mW/cm^2) is lower than the maximum power exposure (MPE) allowed for skin irradiation (18 mW/cm^2), ensuring the biosafety of the light irradiation procedure. Then, the images were acquired at t=10 s after removal of light source using IVIS living imaging system under the bioluminescence mode. As shown in **Figure 4b**, the ultralong phosphorescence of OSN1-T can be easily detected, while it is hardly detectable under the same parameters for OSN1-B. The imaging quantification reveals that the luminescence intensity of OSN1-T is ~22–folder higher than OSN1-B (**Figure 4c**). In contrast, fluorescence imaging is unable to detect for both nanoparticles in living mice (**Figure 4b**). To rule out the possibility that this is because of the relatively lower quantum yields of OSNs, the same *in vivo* luminescence experiments were conducted for the quantum dots (QD520) and fluorescein. As both QD520 and fluorescein emit in the visible region at ~520 nm as OSNs do, the comparison is reasonable. Despite the much higher fluorescent quantum yields of QD520 (25%) and fluorescein (90%) as compared with that of OSN1-T (4.88%), their inclusions are similarly undetectable under both fluorescence and bioluminescence modes (**Figure S11**, Supporting Information). This proves that the strong autofluorescence from the skin of mouse interferes the fluorescence signals of nanoparticles *in vivo*, leading to the undetectability. In contrast, due to the elimination of real-time excitation, the ultralong phosphorescence avoids the autofluorescence and has a really low background noise, making OSN1-T clearly visible in living mice under bioluminescence mode (**Figure 4b**). In addition, the maximum ultralong phosphorescence intensity of OSN-T is 2.0×10^4 p s^{-1} cm^{-2} sr^{-1}, comparable to that of the inorganic ultralong luminescent nanoparticles based on chromiumdoped zinc gallate and poly[2-methoxy-5-(2-ethylhexyloxy)-1,4-phenylenevinylene]-based semiconducting polymer nanoparticles.[11d],[16] A linear correlation between the concentration and ultralong phosphorescence signal of OSN1-T is observed for the tested concentrations ranging from 15 to 1600 nM (**Figure 4d**). As the tissue background is measured to be 458 p s^{-1} cm^{-2} sr^{-1} under

the same signal collection conditions, the detection of limit of OSN1-T in mice using ultralong phosphorescence should be close to 7.5 nM (**Figure S12**, Supporting Information). Similar to the in vitro observation, the ultralong phosphorescence of OSN1-T can be repeatedly activated with no loss in total intensity (**Figure 4e**), showing its capability for longitudinal imaging.

The utility of ultralong phosphorescence of OSN1-T for *in vivo* imaging was further evaluated for real-time mapping of lymph nodes in living mice. Lymph node mapping is clinically important in guiding surgical resection of tumor tissues,[17] which has been rarely demonstrated by optical imaging with no need for real-time external excitation.[18] OSN1-T was administered through intradermal injection into the forepaw of living mice. At t=1 h post-injection, OSN1-T was activated with UV light irradiation for 1 min. Then, the ultralong phosphorescence of OSN1-T was collected at t=10 s after removal of the light source using IVIS living imaging system under bioluminescence mode. As shown in **Figure 4f**, the axillary lymph node could be clearly delineated with ultralong phosphorescence, indicating the efficient accumulation of OSN1-T in sentinel lymph node. This is consistent with the previous studies that nanoparticles with diameters smaller than 100 nm have favourable accumulation and retention in draining lymph nodes.[19] With no autofluorescence, the signal-to-noise ratio for the ultralong phosphorescence guided lymph node imaging is as high as 40, while it is impossible to differentiate the lymph node from the normal tissue using fluorescence imaging (**Figure 4g**). Furthermore, the ex vivo imaging not only confirms the efficient accumulation of OSN1-T in lymph nodes but also demonstrates the effectiveness of the ultralong phosphorescence of OSN1-T for ex vivo tissue imaging (**Figure S13**, Supporting Information).

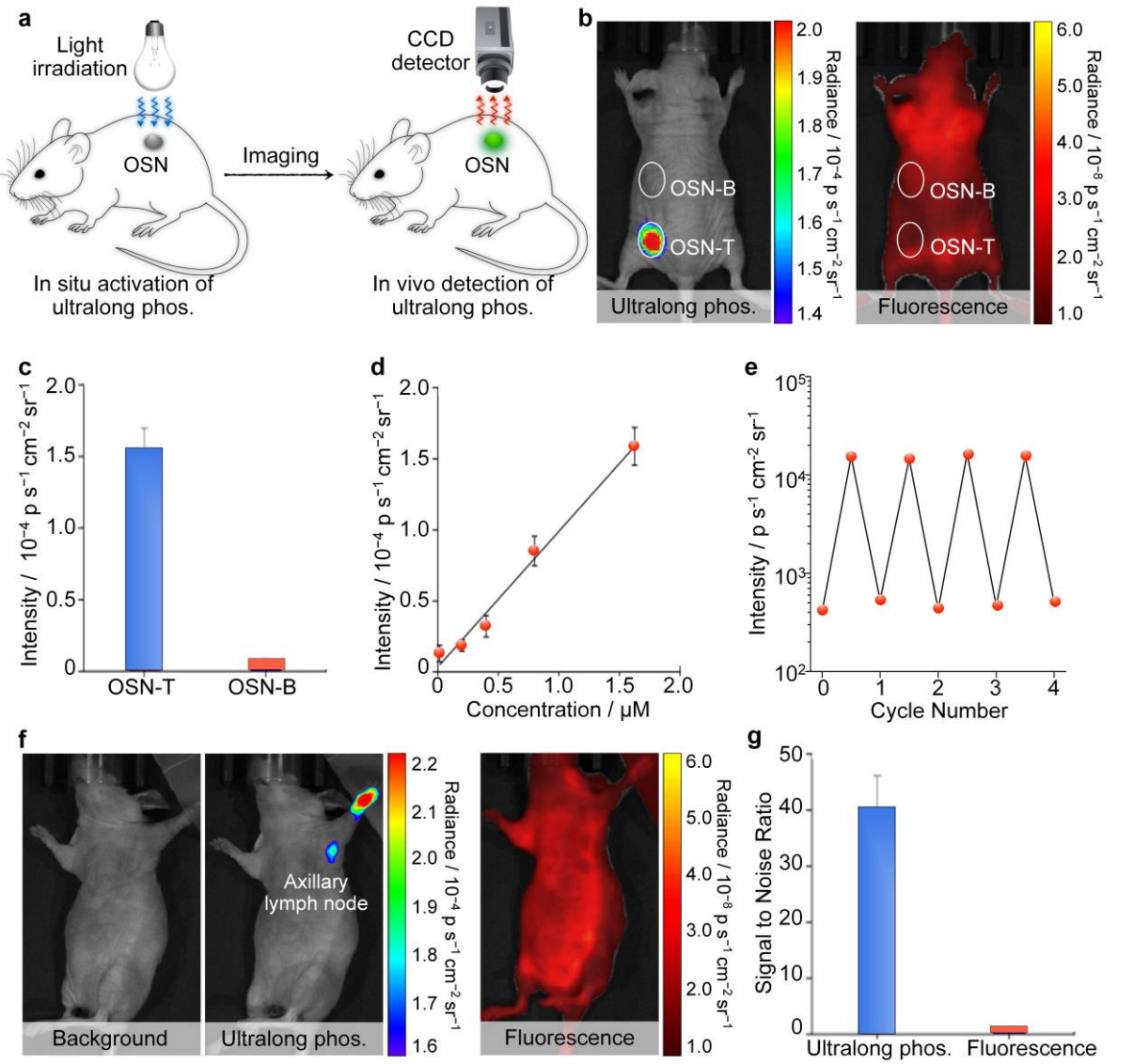

Figure 4. ***In vivo*** **optical imaging of OSNs.** (**a**) Schematic illustration of in situ activation and detection of ultralong phosphorescence of OSNs in living mice. (**b**) Ultralong phosphorescence and fluorescence imaging of a mouse with the subcutaneous inclusions of OSNs (1.6 μM). The circles indicate the location of nanoparticle inclusions. (**c**) Quantification of ultralong phosphorescence of the subcutaneous inclusion of OSNs. (**d**) The *in vivo* intensity of ultralong phosphorescence of the nanoparticle subcutaneous inclusion as a function of the concentration of OSN1-T. (**e**) Ultralong phosphorescence intensities of the subcutaneous inclusion OSN1-T activated repeatedly by UV light (10 mW/cm^2). (**f**) Ultralong phosphorescence and fluorescence imaging of lymph node in living mice 1 h after the intradermal injection of OSN1-T (1.6 μM) into the forepaw of mice. (**g**) Signal-to-noise ratio for ultralong phosphorescence and fluorescence imaging of lymph node in living mice. Error bars were based on standard deviation (n=3).

In summary, we have introduced a top-down method to synthesize water-soluble organic nanoparticles with ultralong luminescent phosphorescent for *in vivo* imaging. With such top-down approach that directly converts the dye solids into the water-soluble nanoparticles, OSNs-T greatly resemble the molecular packing in solid state for better trapping and stabilization of the triplet excited states as compared to OSNs-B synthesized *via* nanoprecipitation method. Such a top-down method enhanced phosphorescence is observed for all three semiconducting dyes, showing their generalizability for other organic luminescent systems. Among all OSNs, OSN1-T emits the strongest ultralong phosphorescence at the time scale that can be detected by the commercially available whole-animal imaging system after removal of external illumination source. Such ultralong phosphorescence is inert to oxygen and water and can be repeatedly activated, making it suitable for long-term imaging in living animals where oxygen and water are ubiquitous. This is also an advantage over bioluminescence or Cerenkov agents that are unable to re-emit light after consumption of substrates or release of nuclear energy, suggesting its obvious advantages and particular usefulness for longitudinal imaging.

The proof-of-concept real-time excitation free imaging application of organic nanoparticles with ultralong phosphorescence has been validated in living mice. The ultralong phosphorescence of OSN1-T can be detected at the concentration as low as 7.5 nM in the subcutaneous tissue of living mice with the brightness comparable to the inorganic persistent luminescent nanoparticles.[11d] With a high sensitivity due to the elimination of tissue autofluorescence, OSN1-T permits afterglow mapping of lymph nodes in living mice at a signal-to-noise ratio of 40. As the design principle leverages aggregation to prolong phosphorescence, it is feasible to develop other organic semiconducting molecules with high tendency to form aggregates for such novel optical imaging modality. The synthetic flexibility of our top-down approach allows to further develop OSNs into smart nanoprobes for targeted imaging, while other nanoparticle formulation methods that can promote the formation of H-aggregates are desired so as to further elongate the luminescence lifetime. Thereby, our study

provides a universal design principle to fill the gap of lacking organic imaging agents with ultralong phosphorescence for *in vivo* imaging.

Supporting Information

Supporting Information is available from the Wiley Online Library or from the author.

Acknowledgements

This work was supported by Nanyang Technological University start-up grant (NTU-SUG: M4081627.120), Academic Research Fund Tier 2 from Singapore Ministry of Education (MOE2014-T2-1-003), Academic Research Fund Tier 1 from Singapore Ministry of Education (M4011559.120, RG133/15), NTU-Northwestern Institute for Nanomedicine (M4081502.F40) and National Natural Science Foundation of China (21674049, 21304049, 61136003 and 2015CB932200).

Received: ((will be filled in by the editorial staff))
Revised: ((will be filled in by the editorial staff))
Published online: ((will be filled in by the editorial staff))

[1] a) V. Ntziachristos, J. Ripoll, L. V. Wang, R. Weissleder, *Nat. Biotechnol.* **2005**, *23*, 313; b) J. F. Lovell, T. W. Liu, J. Chen, G. Zheng, *Chem. Rev.* **2010**, *110*, 2839.

[2] G. M. Van Dam, G. Themelis, L. M. Crane, N. J. Harlaar, R. G. Pleijhuis, W. Kelder, A. Sarantopoulos, J. S. De Jong, H. J. Arts, A. G. Van Der Zee, *Nat. Med.* **2011**, *17*, 1315.

[3] a) X. Zheng, X. Wang, H. Mao, W. Wu, B. Liu, X. Jiang, *Nat. Commun.* **2015**, *6*, 5834 b) J. Chan, S. C. Dodani, C. J. Chang, *Nat. Chem.* **2012**, *4*, 973.

[4] X. Michalet, F. Pinaud, L. Bentolila, J. Tsay, S. Doose, J. Li, G. Sundaresan, A. Wu, S. Gambhir, S. Weiss, *Science* **2005**, *307*, 538.

[5] a) B. Zhou, B. Shi, D. Jin, X. Liu, *Nat. Nanotechnol.* **2015**, *10*, 924; b) W. Fan, W. Bu, J. Shi, *Adv. Mater.* **2016**, *28*, 3987.

[6] X. T. Zheng, A. Ananthanarayanan, K. Q. Luo, P. Chen, *Small* **2015**, *11*, 1620.

[7] a) C. Wu, D. T. Chiu, *Angew. Chem. Int. Ed.* **2013**, *52*, 3086; b) L. Feng, C. Zhu, H. Yuan,

L. Liu, F. Lv, S. Wang, *Chem. Soc. Rev.* **2013**, *42*, 6620; c) K. Pu, J. Mei, J. V. Jokerst, G. Hong, A. L. Antaris, N. Chattopadhyay, A. J. Shuhendler, T. Kurosawa, Y. Zhou, S. S. Gambhir, *Adv. Mater.* **2015**, *27*, 5184; d) K. Pu, A. J. Shuhendler, J. Rao, *Angew. Chem. Int. Ed.* **2013**, *52*, 10325; e) Q. Miao, Y. Lyu, D. Ding, K. Pu, *Adv. Mater.* **2016**, 28, 3662; f) Y. Lyu, Y. Fang, Q. Miao, X. Zhen, D. Ding, K. Pu, *ACS Nano* **2016**, *10*, 4472.

[8] J. Rao, A. Dragulescu-Andrasi, H. Yao, *Curr. Opin. Biotechnol.* **2007**, *18*, 17.

[9] M. K. So, C. Xu, A. M. Loening, S. S. Gambhir, J. Rao, *Nat. Biotechnol.* **2006**, *24*, 339.

[10] H. Liu, X. Zhang, B. Xing, P. Han, S. S. Gambhir, Z. Cheng, *Small* **2010**, *6*, 1087.

[11] a) A. Abdukayum, J.-T. Chen, Q. Zhao, X.-P. Yan, *J. Am. Chem. Soc.* **2013**, *135*, 14125; b) B.-Y. Wu, H.-F, Wang, J.-T. Chen, X.-P. Yan, *J. Am. Chem. Soc.* **2011**, *133*, 686; c) Q.le Masne de Chermont, C. Chanéac, J. Seguin, F. Pellé, S. Maîtrejean, J.-P. Jolivet, D. Gourier, M. Bessodes, D. Scherman, *Proc. Natl. Acad. Sci.* **2007**, *104*, 9266; d) T. Maldiney, A. Bessière, J. Seguin, E. Teston, S. K. Sharma, B. Viana, A. J. Bos, P. Dorenbos, M. Bessodes, D. Gourier, *Nat. Mater.* **2014**, *13*, 418; e) B.-Y. Wu, X.-P. Yan, *Chem. Commun.* **2015**, *51*, 3903; f) Y. Li, M. Gecevicius, J. Qiu, *Chem. Soc. Rev.* **2016,** *45*, 2090; g) Z. Li, Y. Zhang, X. Wu, L. Huang, D. Li, W. Fan, G. Han, *J. Am. Chem. Soc.* 2015, 137, 5304.

[12] a) R. E. Andrews, K. M. Shah, J. M. Wilkinson, A. Gartland, *Bone* **2011,** *49*, 717; b) S. M. Plaza, *Altern. Med. Rev.* **2002,** *7*, 218; c) T. J. Haley, N. Komesu, G. Colvin, L. Koste, H. C. Upham, *J. Pharm. Sci.* **1965,** *54*, 643; d) T. J. Haley, L. Koste, N. Komesu, M. Efros, H. C. Upham, *Toxicol. Appl. Pharm.* **1966,** *8*, 37; e) P. Collery, B. Keppler, C. Madoulet, B. Desoize, *Crit. Rev. Oncol. Hema.* **2002,** *42*, 283.

[13] a) S. Hirata, K. Totani, J. Zhang, T. Yamashita, H. Kaji, S. R. Marder, T. Watanabe, C. Adachi, *Adv. Func. Mater.* **2013**, *23*, 3386; b) O. Bolton, K. Lee, H.-J. Kim, K. Y. Lin, J. Kim, *Nat. Chem.* **2011**, *3*, 205; c) H. Xu, R. Chen, Q. Sun, W. Lai, Q. Su, W. Huang, X. Liu, *Chem. Soc. Rev.* **2014**, *43*, 3259.

[14] a) Z. An, C. Zheng, Y. Tao, R. Chen, H. Shi, T. Chen, Z. Wang, H. Li, R. Deng, X. Liu, W.Huang, *Nat. Mater.* **2015**, *14*, 685. b) S. Xu, R. Chen, C. Zheng, W. Huang, *Adv. Mater.* **2016,** *28*, 9920.

[15] M. Petersilka, U. J. Gossmann, E. K. U. Gross, *Pure Appl. Chem.* **1965**, *11*, 371.

[16] M Palner, K Pu, S Shao, J Jeon, J Rao. *Angew. Chem. Int. Ed.* **2015**, *127*, 11639.

[17] a) S. Kim, Y. T. Lim, E. G. Soltesz, A. M. De Grand, J. Lee, A. Nakayama, J. A. Parker, T. Mihaljevic, R. G. Laurence, D. M. Dor, *Nat. Biotechnol.* **2004**, *22*, 93. b) H. Zhu, Y. Fang, X. Zhen, N. Wei, Y. Gao, K. Q. Luo, C. Xu, H. Duan, D. Ding, P. Chen, K. Pu, *Chem. Sci.* **2016**, *7*, 5118.

[18] K. Pu, N. Chattopadhyay, J. Rao, *J. Control. Release* **2016,** *240*, 312.

[19] K. Pu, A. J. Shuhendler, J. V. Jokerst, J. Mei, S. S. Gambhir, Z. Bao, J. Rao, *Nat. Nanotechnol.* **2014**, *9*, 233.

The table of contents entry: Organic semiconducting nanoparticles were designed to emit afterglow phosphorescence by taking advantage of the strong electron coupling in H-aggregates to greatly stabilize the triplet excited states of a semiconducting phosphorescent molecule. By virtue of the inertness towards oxygen and the ability to be repeatedly activated by light irradiation, the organic semiconducting nanoparticles permit optical imaging of lymph nodes in living mice with no need for real-time light excitation.

Keywords: afterglow, phosphorescence, molecular imaging, organic semiconducting nanoparticles, lymph node imaging

Author: *Xu Zhen*, *Ye Tao*, *Zhongfu An, Peng Chen, Chenjie Xu, Runfeng Chen**, *Wei Huang**, and *Kanyi Pu**

Title: Ultralong Phosphorescence of Water-soluble Organic Semiconducting Nanoparticles for *In Vivo* **Afterglow** Imaging